changes during the transport cycle. In addition, the BtuCD structure clears the way to structural studies of intermediate states, which should further advance our understanding of the translocation mechanisms.

References and Notes

1. See http://ir2lcb.cnrs-mrs.fr/ABCdb/.
2. S. C. Hyde *et al.*, *Nature* **346**, 362 (1990).
3. G. F. Ames *et al.*, *FEMS Microbiol. Rev.* **75**, 429 (1990).
4. D. N. Sheppard, M. J. Welsh, *Physiol. Rev.* **79**, S23 (1999).
5. M. M. Gottesman, S. V. Ambudkar, *J. Bioenerg. Biomembr.* **33**, 453 (2001).
6. R. Abele, R. Tampe, *Biochim. Biophys. Acta* **1461**, 405 (1999).
7. A. Kelly *et al.*, *Nature* **355**, 641 (1992).
8. W. Boos, J. M. Lucht, in Escherichia coli *and* Salmonella typhimurium: *Cellular and Molecular Biology*, F. C. Neidhardt *et al.*, Eds. (American Society for Microbiology, Washington, DC, 1996), vol. 1, pp. 1175–1209.
9. H. Nikaido, *Science* **264**, 382 (1994).
10. J. E. Walker *et al.*, *EMBO J.* **1**, 945 (1982).
11. E. Schneider, S. Hunke, *FEMS Microbiol. Rev.* **22**, 1 (1998).
12. I. B. Holland, M. A. Blight, *J. Mol. Biol.* **293**, 381 (1999).
13. K. P. Hopfner *et al.*, *Cell* **101**, 789 (2000).
14. F. A. Quiocho, P. S. Ledvina, *Mol. Microbiol.* **20**, 17 (1996).
15. I. L. Urbatsch *et al.*, *J. Biol. Chem.* **270**, 19383 (1995).
16. J. Chen *et al.*, *Proc. Natl. Acad. Sci. U.S.A.* **98**, 1525 (2001).
17. H. W. van Veen *et al.*, *EMBO J.* **19**, 2503 (2000).
18. L. W. Hung *et al.*, *Nature* **396**, 703 (1998).
19. K. Diederichs *et al.*, *EMBO J.* **19**, 5951 (2000).
20. R. Gaudet, D. C. Wiley, *EMBO J.* **20**, 4964 (2001).
21. N. Karpowich *et al.*, *Structure* **9**, 571 (2001).
22. Y. R. Yuan *et al.*, *J. Biol. Chem.* **276**, 32313 (2001).
23. G. Chang, C. B. Roth, *Science* **293**, 1793 (2001).
24. M. F. Rosenberg *et al.*, *EMBO J.* **20**, 5615 (2001).
25. M. F. Rosenberg *et al.*, *J. Biol. Chem.* **276**, 16076 (2001).
26. G. Chang, *Science* **282**, 2220 (1998).
27. Materials and methods are available as supporting material on *Science* Online at www.sciencemag.org/cgi/content/full/296/5570/1091/DC1.
28. P. R. Reynolds, G. P. Mottur, C. Bradbeer, *J. Biol. Chem.* **255**, 4313 (1980).
29. L. C. DeVeaux, R. J. Kadner, *J. Bacteriol.* **162**, 888 (1985).
30. E. Heath, O. W. Howarth, *J. Chem. Soc.-Dalton Trans.*, 1105 (1981).
31. W. Groeger, W. Koster, *Microbiology* **144**, 2759 (1998).
32. B. Lankat-Buttgereit, R. Tampe, *Physiol. Rev.* **82**, 187 (2002).
33. N. Cadieux *et al.*, *J. Bacteriol.* **184**, 706 (2002).
34. M. Mourez, N. Hofnung, E. Dassa, *EMBO J.* **16**, 3066 (1997).
35. J. F. Cotten *et al.*, *J. Biol. Chem.* **271**, 21279 (1996).
36. S. J. Currier *et al.*, *J. Biol. Chem.* **267**, 25153 (1992).
37. B. S. Kerem *et al.*, *Proc. Natl. Acad. Sci. U.S.A.* **87**, 8447 (1990).
38. L. C. Tsui, *Trends Genet.* **8**, 392 (1992).
39. H. L. Chen *et al.*, *Nature Genet.* **13**, 210 (1996).
40. L. Saveanu *et al.*, *J. Biol. Chem.* **276**, 22107 (2001).
41. K. P. Locher *et al.*, *Cell* **95**, 771 (1998).
42. A. D. Ferguson *et al.*, *Science* **282**, 2215 (1998).
43. P. J. Thomas, J. F. Hunt, *Nature Struct. Biol.* **8**, 920 (2001).
44. A. L. Davidson *et al.*, *Proc. Natl. Acad. Sci. U.S.A.* **89**, 2360 (1992).
45. C. F. Higgins, M. M. Gottesman, *Trends Biochem. Sci.* **17**, 18 (1992).
46. H. Schindelin *et al.*, *Nature* **387**, 370 (1997).
47. W. Koster, *Res. Microbiol.* **152**, 291 (2001).
48. Z. Otwinowski, W. Minor, *Methods Enzymol.* **276**, 307 (1997).
49. D. E. McRee, *J. Struct. Biol.* **125**, 156 (1999).
50. T. C. Terwilliger, J. Berendzen, *Acta Crystallogr.* **D55**, 849 (1999).
51. E. de la Fortelle, G. Bricogne, *Methods Enzymol.* **276**, 472 (1997).
52. CCP4, *Acta Crystallogr.* **D50**, 760 (1994).
53. T. A. Jones *et al.*, *Acta Crystallogr.* **A47**, 110 (1991).
54. A. T. Brünger *et al.*, *Acta Crystallogr. D Biol. Crystallogr.* **54**, 905 (1998).
55. M. T. Averbuchpouchot, A. Durif, *Eur. J. Solid State Inorg. Chem.* **31**, 567 (1994).
56. R. A. Laskowski *et al.*, *J. Appl. Crystallogr.* **26**, 283 (1993).
57. Single-letter abbreviations for the amino acid residues are as follows: A, Ala; C, Cys; D, Asp; E, Glu; F, Phe; G, Gly; H, His; I, Ile; K, Lys; L, Leu; M, Met; N, Asn; P, Pro; Q, Gln; R, Arg; S, Ser; T, Thr; V, Val; W, Trp; and Y, Tyr.
58. See www.dino3d.org.
59. M. F. Sanner *et al.*, *Biopolymers* **38**, 305 (1996).

60. We thank the staff at the Stanford Synchrotron Radiation Laboratory (SSRL), the Advanced Photon Source (APS), the Advanced Light Source (ALS), and the National Synchrotron Light Source (NSLS) for their support during crystal screening and data collection. We also thank M. Barclay, R. Bass, O. Einsle, I. Locher-Hinderling, and P. Strop for helpful discussions. We further thank M. Day for assistance in obtaining the cyclotetravanadate coordinates, and L. Ackerman and J. Bercaw for their help in the synthesis of inorganic clusters during the search for derivatives. The coordinates of the BtuCD transporter with bound cyclotetravanadate have been deposited in the Protein Data Bank (www.rcsb.org/pdb) with access code IL7V.

21 February 2002; accepted 21 March 2002

REPORTS

Scanned Probe Imaging of Single-Electron Charge States in Nanotube Quantum Dots

Michael T. Woodside[1] and Paul L. McEuen[2]

An atomic force microscope was used to study single-electron motion in nanotube quantum dots. By applying a voltage to the microscope tip, the number of electrons occupying the quantum dot could be changed, causing Coulomb oscillations in the nanotube conductance. Spatial maps of these oscillations were used to locate individual dots and to study the electrostatic coupling between the dot and the tip. The electrostatic forces associated with single electrons hopping on and off the quantum dot were also measured. These forces changed the amplitude, frequency, and quality factor of the cantilever oscillation, demonstrating how single-electron motion can interact with a mechanical oscillator.

Single-electron charging phenomena are ubiquitous in atoms, molecules, and small electronic devices, and their effects are central to an understanding of the physics and technology of nanoscale systems. Single-electron effects arise because the number of electrons residing on a small, quasi-isolated, conducting island is quantized. Adding an additional charge to such a quantum dot costs an electrostatic energy on the order of $U = e^2/C$, where C is the capacitance of the dot and e is the electronic charge (*1*). This charging energy suppresses charge transport when $U \gg k_BT$, where k_BT is the thermal energy, leading to the Coulomb blockade of charge motion on and off the dot.

Although Coulomb blockade phenomena have been studied extensively with transport measurements (*2*), such measurements lack the spatial discrimination necessary to probe the interior of a dot or to probe complex multidot systems. An alternative approach is to detect single-charge motion using scanned probe techniques, such as scanned capacitance microscopy (*3*, *4*), scanned single-electron transistors (*5*, *6*), and atomic force microsopy (AFM). The first two of these have excellent charge sensitivity but are technically very difficult; moreover, they are not easily able to image the topography of the device under study. AFM-based techniques, on the other hand, can be used both to image the sample and to interact with it in a variety of ways. For example, electrostatic force microscopy (EFM), which measures the electrostatic force between a sample and a metallized AFM tip, has been used to detect the motion of single charges during contact electrification of insulating surfaces (*7*) and to image the potential profile in carbon nanotubes (*8*). In addition, scanned gate microsopy (SGM), in which the AFM tip is used to perturb the conducting properties of a sample, has been used to image electron trajectories and scattering centers in two-dimensional electron gases (*9*–*11*) and barriers in carbon nanotubes (*8*, *12*, *13*).

[1]Department of Physics, University of California, Berkeley, CA 94720, USA. [2]Laboratory of Atomic and Solid State Physics, Cornell University, Ithaca, NY 14853, USA.

We describe experiments that extend these AFM-based techniques into the single-electron regime, by using a low-temperature AFM (*14*) to perform single-electron scanned gate microscopy (*e*-SGM) and single-electron electrostatic force microscopy (*e*-EFM). The samples we study are individual single-walled carbon nanotubes grown by chemical vapor deposition (*15*) on a backgated Si substrate and attached to electrical contacts (*16*). Tunnel barriers arising from defects and/or imperfect electrical contacts to the nanotube define quantum dots in the tube (*13*, *16*, *17*). The charge state of a dot is controlled by changing either the position or the voltage of the AFM tip relative to the dot (Fig. 1, top). This charge state is then probed by monitoring the conductance of the dot (*e*-SGM) or the mechanical oscillation of the AFM cantilever (*e*-EFM). These measurements allow us to explore not only the local properties of nanotube quantum dots but also the influence of single-electron motion on a mechanical oscillator.

We begin by discussing *e*-SGM, in which the charge state of a quantum dot is sensed by transport measurements. An *e*-SGM measurement of the conductance of a metallic nanotube device as a function of the tip voltage V_{tip} is shown in Fig. 1A, made at $T = 0.6$ K when the position of the AFM tip is fixed 120 nm above the tube (*18*). The sharp peaks observed in the conductance are the Coulomb oscillations that occur at low temperature ($k_BT \ll U$) each time a single electron is added to a dot in the nanotube (*1*). These Coulomb oscillations arise because the tip voltage would like to induce a continuous charge q (the "control charge") on the dot, but the charge e that can actually be transferred to the dot is quantized. This produces periodic steps in the occupancy of the dot as a function of the gate voltage (Fig. 1A), resulting in peaks in the conductance each time an electron is added to the dot.

The control charge q induced on the dot by the AFM tip is given by:

$$q(\vec{r},\Delta V) = C_{td}(\vec{r}) \cdot \Delta V \qquad (1)$$

where $C_{td}(\vec{r})$ is the tip-dot capacitance as a function of the tip position $\vec{r}$, and $\Delta V = V_{tip} - V_{dot} - \Phi_{td}$ is the electrostatic potential difference between the tip and the dot ($\Phi_{td} \sim 0.2$ to 0.3 V is the work function difference between the tip and the dot). The conductance of the dot can thus be changed not only by varying V_{tip} but also by moving the tip over the sample. Imaging the conductance of the device as a function of the tip position in (x,y) for fixed $V_{tip} = -200$ mV (Fig. 2A), we observe two sets of concentric rings of conductance peaks, centered at different locations on the nanotube. Each ring in the image corresponds to a single Coulomb oscillation on the dot enclosed by the ring: it is the locus of tip positions that correspond to the particular control charge producing the conductance peak. As the tip approaches the dot, C_{td} grows, causing the negative tip bias to push electrons off the dot one by one, producing successive concentric rings.

The two sets of rings in Fig. 2A indicate that there are two quantum dots in series along the tube, located at the center of each set of rings. A defect or local potential perturbation in this nanotube apparently creates a tunnel barrier that breaks the tube into two dots (*13*, *19*). The size of the elliptically shaped Coulomb oscillations for the dot on the right side of Fig. 2A indicates a dot of length $L \sim 1.5$ μm, which corresponds well to the length of 1 to 2 μm that is inferred from the data in Fig. 1A (*16*, *17*). The rings around the dot on the left side are further apart and nearly perfectly circular, indicating that this dot is significantly smaller ($L \lesssim 0.7$ μm). These *e*-SGM images thus give valuable spatial information about the location and size of the quantum dots formed in nanotubes.

We next consider *e*-EFM measurements, in which we measure the dynamical response of the AFM cantilever to the force from single-electron motion. The cantilever responds to an external driving force F_{ext} as a damped simple harmonic oscillator (*20*). The

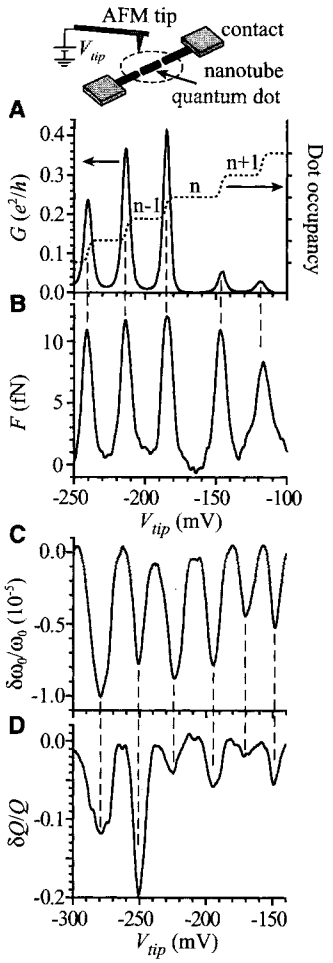

Fig. 1. Single-electron AFM measurements of Coulomb oscillations as a function of V_{tip}. (Top) Measurement confuguration. Tunnel barriers in the carbon nanotube create quantum dots. The dot occupancy is controlled by changing either the dc bias V_{tip} on the AFM tip or the position of the tip with respect to the dot. The dashed line shows tip positions that produce a constant dot occupancy for a given V_{tip}. (**A**) *e*-SGM measurement of the conductance of a nanotube quantum dot at 0.6 K. Peaks occur each time a single electron is added to the dot. The dot occupancy is shown with a dotted line. n is an integer number of electrons on the dot. (**B**) *e*-EFM measurement of the force from single-electron charging on the same dot, under the same conditions. Peaks in the force occur at the same location as the peaks in the conductance. (**C** and **D**) *e*-EFM measurements of the fractional change in the resonant frequency (C) and Q (D) of the cantilever, for a different device. Both the frequency and Q decrease at the Coulomb oscillations because of the single-electron motion.

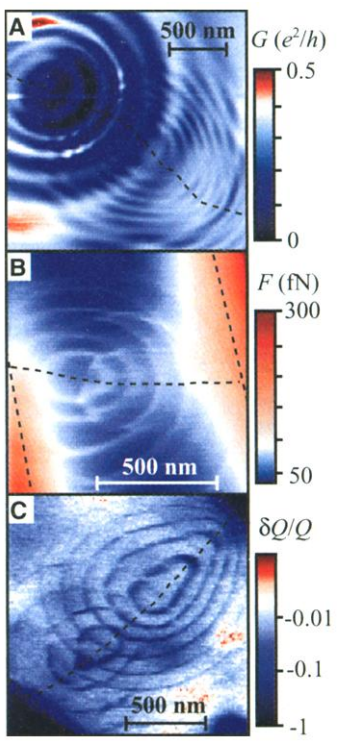

Fig. 2. Coulomb oscillations as a function of tip position. In all images, dashed lines show the location of the nanotube and contacts, determined from topographic AFM scans. (**A**) An *e*-SGM image of the conductance reveals two sets of concentric rings of conductance peaks from Coulomb oscillations on two dots in series in this nanotube. $T \sim 6$ K, $V_{tip} = -200$ mV. (**B**) An *e*-EFM image of the force from a different device. An ac voltage at the resonant frequency of the cantilever is applied to the sample electrodes. Concentric rings of force peaks are seen, enclosing two dots in series. $T = 0.6$ K, $V_{tip} = -400$ mV. (**C**) An *e*-EFM image of the Q degradation from a third device. Two sets of concentric rings where the Q is reduced enclose two dots in series. $T = 0.6$ K, $V_{tip} = -300$ mV.

force driving the cantilever in *e*-EFM is the electrostatic force exerted on the tip by a single electron moving on/off the quantum dot. This charge motion produces a change U/e in the electrostatic potential of the dot, which in turn exerts a force F_e on the tip (*21*)

$$F_e = C'_{td}(\Delta V \cdot U/e) \quad (2)$$

where $C'_{td} = dC_{td}/dz$ is the derivative of the tip-dot capacitance. For typical parameters [$\Delta V \sim 0.5$ V, $U/e = 2$ mV, and $C'_{td} = 3 \times 10^{-11}$ F/m (*22*)], we expect $F_e \sim 30$ fN. This force is two orders of magnitude larger than the sensitivity of the AFM on resonance ($F_{min} \sim 0.3$ fN/$\sqrt{\text{Hz}}$) (*14*, *21*), hence single-electron forces should be readily detectable (*23*).

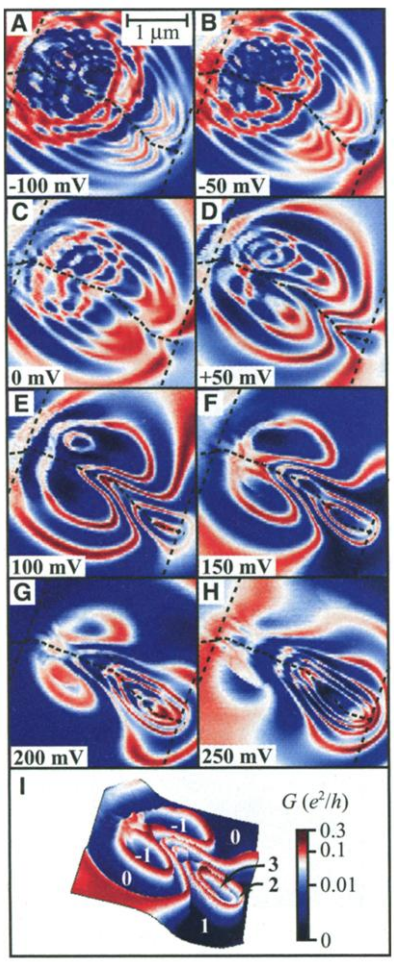

Fig. 3. (**A** to **H**) Evolution of *e*-SGM features with tip voltage. In all images, dashed lines show the location of the nanotube and contacts. At large negative V_{tip}, concentric rings are seen as electrons are removed from the dot as the tip approaches. At large positive V_{tip}, rings are seen as electrons are added to the dot as the tip approaches. At $V_{tip} \sim 100$ to 200 mV, the behavior is complex, and several noncircular features can be observed. (**I**) Charge occupancy of dot inferred from image at $V_{tip} = 150$ mV. The tip can either increase or decrease the occupancy of the dot, depending on its position, as it screens the dot from its electrostatic environment.

To measure the single-electron force, we push an electron on/off the dot at the resonant frequency ω_0 of the cantilever by oscillating at ω_0 either the voltage between the tip and the dot or the height of the tip above the dot. A control charge modulation of $\delta q(\omega_0)$ changes the occupancy of the dot by $df(\omega_0) = (df/dq)\delta q(\omega_0)$, where f is the probability that the dot is occupied (*24*), producing a force

$$F(\omega_0) = (df/dq)\delta q(\omega_0)F_e \quad (3)$$

df/dq has sharp peaks as a function of the control charge at the same locations as the Coulomb oscillations in transport (*1*). We therefore expect Coulomb oscillations in the force exerted by the dot.

We look first at *e*-EFM measurements, using the tip-dot voltage to change the charge state of the dot. We apply a small ac voltage $V(\omega_0) = 0.7$ mV to the contacts of the nanotube (*25*), changing the control charge on the dot by $\delta q(\omega_0) \sim 0.1\ e$. The amplitude of the resulting force on the AFM tip as a function of V_{tip}, measured under the same conditions as the *e*-SGM trace in Fig. 1A, is shown in Fig. 1B. We observe sharp peaks in the force that align with the Coulomb oscillations in the transport. These peaks represent the force on the tip from a single electron moving on/off the dot. The expected peak amplitude, using $edf/dq_{max} \sim 5$ (calculated from the conductance measurement in Fig. 1A), is $F_{max}(\omega_0) \sim 15$ fN, in good agreement with the measured result of ~12 fN.

The single-electron force can also be measured when the occupancy of the dot is changed not by applying ac voltages to the sample but by oscillating the height of the AFM tip above the dot. In this case, the ac motion of the dc-biased tip pushes electrons on and off the dot at the resonant frequency of the cantilever. We drive the cantilever mechanically at ω_0 with a fixed force, using a piezoelectric element at the base of the cantilever that is part of a self-resonant loop (*14*), and we then monitor both the frequency ω_0 and the quality factor Q of the cantilever resonance. Measurements of the fractional changes $\delta\omega_0/\omega_0$ and $\delta Q/Q$ are shown as a function of V_{tip} for a second nanotube device (Fig. 1, C and D). Dips in both ω_0 and Q are observed at the Coulomb oscillations: Single-electron motion decreases the cantilever's natural oscillation frequency and leads to additional energy dissipation. Measurements on a number of dots show that the size of the frequency shift signal is similar on different dots ($\delta\omega_0/\omega_0 \sim 5 \times 10^{-6}$ to 5×10^{-5} at $\Delta V \sim 0.5$ V), whereas the variation in Q degradation is very large ($\delta Q/Q \sim 0.02$ to 0.5 at $\Delta V \sim 0.5$ V).

These effects can be understood by noting that the small periodic motion of the AFM tip $z(\omega_0)$ produces a periodic change in the control charge $\delta q(\omega_0) = \Delta V C'_{td}\, z(\omega_0)$, and hence from Eq. 3 a force proportional to z that modifies the dynamic properties of the cantilever. Taking into account the phase lag between the charge motion and the tip motion due to the finite rate Γ at which electrons tunnel on/off the dot, this force has both real (in-phase) and imaginary (out-of-phase) components

$$F(\omega_0) \sim \delta k \cdot z(\omega_0)\left(1 - \frac{i\omega_0}{\Gamma}\right),$$

$$\text{where } \delta k = -\frac{(F_e^2/U)(edf/dq)}{1 - (\omega_0/\Gamma)^2} \quad (4)$$

For a nanotube quantum dot of length ~1 μm, we estimate $\Gamma \sim (10^{12}\ \text{s}^{-1})\,\mathcal{T}$, where $\mathcal{T}$ is the transmission coefficient for tunneling off the dot. The ratio $\omega_0/\Gamma \sim 10^{-7}/\mathcal{T}$ is very small, except for very opaque barriers.

The real part of the force in Eq. 4 corresponds to an additional effective spring constant for the cantilever δk, producing a resonant frequency decrease $\delta\omega_0/\omega_0 = \delta k/2k$. Physically, as the tip approaches the sample during each cycle of the oscillation, the additional charge induced on the dot pulls the tip toward the dot, slowing down the oscillation and reducing ω_0. The magnitude expected for typical parameters is $(\delta\omega_0/\omega_0)_{max} \sim 5 \times 10^{-6}$, in good agreement with the observed values.

The imaginary part of the force in Eq. 4 corresponds to an effective damping term, producing a decrease in Q given by $\delta(1/Q) \sim (-\delta k/k)(\omega_0/\Gamma)$. Physically, this additional energy dissipation is due to the resistive losses from single electrons moving on and off the dot during the cantilever oscillations. It is a manifestation of the well-known fluctation-dissipation theorem, which requires that the energy delivered to the cantilever by the fluctuating single-electron forces be balanced by additional dissipation. The single-electron dissipation depends inversely on $\mathcal{T}$, becoming maximal when the time for hopping on/off the dot is comparable to the oscillation frequency of the cantilever ($\mathcal{T} \sim 10^{-7}$). This hopping rate can vary by orders of magnitude from one dot to the next (or even from one Coulomb oscillation to the next in the same dot). There are therefore large variations in the magnitude of the Q degradation signal for different dots or even for different Coulomb oscillations in the same dot (Fig. 1D) (*26*).

Just as with *e*-SGM, *e*-EFM can also be used to make images of the charge state of a quantum dot as a function of the tip position. In Fig. 2B, the single-electron force is measured on a different nanotube by applying an ac voltage $V(\omega_0)$ to the sample electrodes. Concentric rings of peaks in the force on the AFM tip are observed, centered on the nanotube. As with the rings in the conductance in Fig. 2A, each ring corresponds to a change of a single electron in the charge state of the quantum dot at the center of the rings. Figure 2C shows a measurement of the Q degradation as a function of tip position for yet another nanotube. Two sets of well-

defined concentric rings of Q degradation centered at two different locations in the nanotube are observed, corresponding to two distinct quantum dots. No electrical signal needs to be applied to the tube in this measurement, making it possible to measure tubes that are not electrically connected to external wires (*27*). Measurements on a number of samples show that multiple-dot behavior is quite common, with dot sizes ranging from <0.2 μm to >1.5 μm (with an average of 0.5 μm) in the six devices studied.

Finally, we turn our attention to the electrostatic information about the device that can be obtained by monitoring the charge state of the dot while varying both the tip position and the tip voltage. We restrict our discussion to *e*-SGM, but our comments are valid for the *e*-EFM techniques as well. A sequence of *e*-SGM images at different values of V_{tip} is shown in Fig. 3, concentrating on the dot on the right side of Fig. 2A. At large negative V_{tip} (Fig. 3A), a series of rings is seen that corresponds to the removal of electrons from the dot as the tip approaches the dot, whereas at large positive V_{tip} (Fig. 3H), concentric rings corresponding to the addition of electrons are seen. The features evolve continuously with V_{tip} between these limits but become complex near $V_{tip} \sim 100$ mV. For example, in Fig. 3I we show the number of electrons induced on the dot as a function of tip position at $V_{tip} = 150$ mV. We see that the tip can either add or subtract electrons from the dot, depending on its position.

A full explanation of the behavior shown in Fig. 3 is beyond the scope of this report, but its origin can be understood qualitatively by considering the effects of the electrostatic environment of the quantum dot. In addition to the charge induced on the dot by the AFM tip, charge is also induced by electric fields from the contacts, the backgate, and any fixed charges nearby on the sample. As the conducting tip moves over the sample, it screens these fields, changing the charge induced on the dot by the environment. It is the screening of these fields that gives rise to the complex spatial variation in the charge states of the dot. The effects of screening are most pronounced when the electrostatic potential difference between the tip and the dot is close to zero (here, when $V_{tip} \sim$ 100 to 200 mV). In this situation, the tip has little direct effect on the dot; instead, its main effect is to screen the dot from its electrostatic environment. This result emphasizes an important lesson: Although scanned probe techniques have the exquisite sensitivity needed to image single electrons in nanostructures, they almost invariably alter the properties of the system they are measuring (*4*, *6*, *11*).

References and Notes

1. H. Grabert, M. H. Devoret, Eds., *Single Charge Tunneling* (Plenum, New York, 1992).
2. L. P. Kouwenhoven *et al.*, in *Mesoscopic Electron Transport*, L. L. Sohn, L. P. Kouwenhoven, G. Schön, Eds. (Kluwer, Dordrecht, Netherlands, 1997).
3. S. H. Tessmer, P. I. Glicofridis, R. C. Ashoori, L. S. Levitov, M. R. Melloch, *Nature* **392**, 51 (1998).
4. G. Finkelstein, P. I. Glicofridis, R. C. Ashoori, M. Shayegan, *Science* **289**, 90 (2000).
5. M. J. Yoo *et al.*, *Science* **276**, 579 (1997).
6. N. B. Zhitenev *et al.*, *Nature* **404**, 473 (2000).
7. C. Schönenberger, S. F. Alvarado, *Phys. Rev. Lett.* **65**, 3262 (1990).
8. A. Bachtold *et al.*, *Phys. Rev. Lett.* **84**, 6082 (2000).
9. R. Crook, C. G. Smith, M. Y. Simmons, D. A. Ritchie, *J. Phys. C* **12**, L167 (2000).
10. M. A. Topinka *et al.*, *Science* **289**, 2323 (2000).
11. M. T. Woodside *et al.*, *Phys. Rev. B* **64**, 1310 (2001).
12. S. J. Tans, C. Dekker, *Nature* **404**, 834 (2000).
13. M. Bockrath, W. J. Liang, D. Bozovic *et al.*, *Science* **291**, 283 (2001).
14. K. L. McCormick *et al.*, *Phys. Rev. B* **59**, 4654 (1999).
15. J. Kong, H. T. Soh, A. M. Cassell, C. F. Quate, H. J. Dai, *Nature* **395**, 878 (1998).
16. M. Bockrath *et al.*, *Science* **275**, 1922 (1997).
17. S. J. Tans *et al.*, *Nature* **386**, 474 (1997).

18. When the tip is very close to the surface, it occasionally causes surface charges to move, producing irreversible changes in the device properties. All measurements are therefore made at heights above 100 nm.
19. We observe no obvious topographic features in the tube between the dots, where the tunnel barrier is located.
20. A typical cantilever used in these measurements has a resonant frequency $\omega_0 \sim 2 \times 10^5$ s^{-1}, a spring constant $k \sim 3$N/m, and a quality factor $Q \sim 30{,}000$.

21. D. Sarid, *Scanning Force Microscopy* (Oxford Univ. Press, Oxford, 1994).

22. C'_{td} is determined from *e*-SGM measurements of C_{td} as a function of the tip height.
23. The sensitivity expressed as a function of charge for the conditions here is ~0.03*e*, comparable to that of other scanned probe techniques that have been used to sense single charges (*3*, *5*). *e*-EFM measurements do perturb the charge on the dot, because of the dc tip-dot bias ΔV. The smallest ΔV practical for measurements is ~100 mV, which adds about four electrons to the dot. This is the same size of perturbation that results from the screening of the electrostatic environment of the dot, so *e*-EFM is not much more perturbative than any conducting scanned probe tip would be.
24. The derivative df/dq can be obtained from the conductance G, because each conductance peak has the form $G(q) = G_{max} \cdot (edf/dq)$ (*1*). For transport through a single energy level, f is just the Fermi distribution function.
25. The voltage is applied to the electrodes, and not the tip, for experimental convenience.
26. For a highly conducting dot like the one shown in Fig. 1A ($\mathcal{T} \sim 0.1 - 0.01$), Eq. 4 predicts an immeasurably small Q degradation ($\delta Q/Q \sim 10^{-5}$ to 10^{-6}). In fact, however, we observe a small but measurable signal ($\delta Q/Q \sim 0.02$). This indicates that other dissipative processes are also present in the experiment. For example, nonlinear electrostatic interactions between the tip and dot may produce coupling to other vibrational modes of the cantilever.
27. This is the case if the dot is electrically connected to somewhere the electron can go, such as another quantum dot or a single contact.

28. We thank J. Park, P. Kim, C. Vale, and M. Fuhrer for help with device preparation. Supported by the U.S. Department of Energy, Basic Energy Sciences, Materials Science Division, sp^2 Materials Initiative; and NSF.

16 January 2002; accepted 4 April 2002

Creation and Manipulation of Three-Dimensional Optically Trapped Structures

M. P. MacDonald,[1] L. Paterson,[1] K. Volke-Sepulveda,[2] J. Arlt,[3] W. Sibbett,[1] K. Dholakia[1]*

An interferometric pattern between two annular laser beams is used to construct three-dimensional (3D) trapped structures within an optical tweezers setup. In addition to being fully translatable in three dimensions, the trapped structure can be rotated controllably and continuously by introducing a frequency difference between the two laser beams. These interference patterns could play an important role in the creation of extended 3D crystalline structures.

At a microscopic level, transparent objects can be trapped and manipulated using the forces exerted by a tightly focused laser beam. This technique, known as "optical tweezers" (*1*, *2*), has enabled major advances in numerous areas of science, including force detection measurements on biological samples, such as the determination of the elastic response of DNA (*3*). Recent work has also demonstrated the use of optical tweezers for developing optical micromachines and micro-components (*4*–*8*). In parallel with this, the extension of optical tweezers to multiple beam sites to create two-dimensional particle arrays (*9*, *10*) has been investigated. We take this technique a step further by creating vertical arrays of particles (stacking) in multiple trapping sites, forming the basis for creating 3D trapped structures.

Stacking of a small number of particles in standing-wave geometries (*11*) and Bessel light beams (*12*) has been observed experimentally, whereas Gauthier and Ashman theoretically predicted stacking in a Gaussian beam (*13*). Experimentally, we have observed controlled stacking of large numbers of particles in optical tweezers using a single Gaussian beam. By extending this to multiple trapping sites, formed in the interference pattern generated between two annular (Laguerre-Gaussian) light beams, we have created 3D trapped structures. Furthermore, we use the angular Doppler effect to achieve continuous and controlled rotation of the 3D structure.

The mechanism for creating particle stacks